ARL-TN-0968 ● Sep 2019

Stack Reconstruction of Noisy High Contrast Microstructural Images for High-throughput Characterization

by Efraín Hernández-Rivera and Jonathan P Ligda

NOTICES

Disclaimers

ARL-TN-0968 ● SEP 2019

Stack Reconstruction of Noisy High Contrast Microstructural Images for High-throughput Characterization

by Efraín Hernández-Rivera and Jonathan P Ligda
Weapons and Materials Research Directorate, CCDC Army Research Laboratory

REPORT DOCUMENTATION PAGE	*Form Approved* *OMB No. 0704-0188*

1. REPORT DATE *(DD-MM-YYYY)*	**2. REPORT TYPE**	**3. DATES COVERED (From - To)**
September 2019	Technical Note	June 2018; August 2019-September 2019

4. TITLE AND SUBTITLE	**5a. CONTRACT NUMBER**
Stack Reconstruction of Noisy High Contrast Microstructural Images for High-throughput Characterization	
	5b. GRANT NUMBER
	5c. PROGRAM ELEMENT NUMBER
6. AUTHOR(S)	**5d. PROJECT NUMBER**
Efraín Hernández–Rivera and Jonathan P Ligda	**5e. TASK NUMBER**
	5f. WORK UNIT NUMBER
7. PERFORMING ORGANIZATION NAME(S) AND ADDRESS(ES)	**8. PERFORMING ORGANIZATION REPORT NUMBER**
US Army Combat Capabilities Development Command Army Research Laboratory ATTN: FCDD-RLW-MB Aberdeen Proving Ground, MD 21005-5066	ARL-TN-0968
9. SPONSORING/MONITORING AGENCY NAME(S) AND ADDRESS(ES)	**10. SPONSOR/MONITOR'S ACRONYM(S)**
	11. SPONSOR/MONITOR'S REPORT NUMBER(S)

12. DISTRIBUTION/AVAILABILITY STATEMENT

Approved for public release; distribution is unlimited.

13. SUPPLEMENTARY NOTES

primary author's email: <efrain.hernandez18.civ@mail.mil>.

14. ABSTRACT

Technological advancements have enabled the collection of large experimental microstructural data sets. A recently developed infrastructure at the US Army Combat Capabilities Development Command (CCDC) Army Research Laboratory enables characterization of 3D microstructures through femtosecond laser sectioning. This information is useful in understanding a material's microstructural complexity, often unattainable from 2D micrographs. A systematic framework to clean noisy micrographs, reconstruct individual micrograph frames into an image stack, and post-process the resulting 3D microstructure is presented. To showcase the importance of this type of analysis, a micromechanical analysis of a simplified microstructure is performed.

15. SUBJECT TERMS

image segmentation, stack reconstruction, post-processing framework

16. SECURITY CLASSIFICATION OF:			**17. LIMITATION OF ABSTRACT**	**18. NUMBER OF PAGES**	**19a. NAME OF RESPONSIBLE PERSON**
					Efraín Hernández–Rivera
a. REPORT	**b. ABSTRACT**	**c. THIS PAGE**			**19b. TELEPHONE NUMBER (Include area code)**
Unclassified	Unclassified	Unclassified	UU	19	410-306-4961

Standard Form 298 (Rev. 8/98)
Prescribed by ANSI Std. Z39.18

Contents

List of Figures

1. Introduction

The emergence of high-throughput (HiTp) methodologies in materials science results in the need of efficient frameworks capable of collecting, storing, and analyzing large data sets. From a material science perspective, HiTp has traditionally focused on the development of computational tools[1,2] since HiTp experimental (HiTpE) approaches present many challenges. While many great advancements and discoveries have been enabled through computational materials science, any model is only as good as its least accurate assumption. Therefore, the development of HiTpE methods is essential to overcoming limitations inherent to computational materials science. In fact, HiTpE has taken a greater significance as the main approach to achieving the accelerated materials discovery goals set forward by the Material Genome Initiative.[3,4]

Recent advancements in automation and computing resources have enabled the development of true HiTpE methodologies as applied to materials science. While great progress has been made on HiTpE methods for 1D data (e.g., spectral[5,6] and/or patterns[7,8]), these reduced-order data type only provide limited information. Furthermore, these usually analyze small volumes of material, which have limited applications within the scope of the Army. For example, HiTp X-ray diffraction typically consists of analyzing deposited thin films with compositional variations across the deposition substrate.[7,8] Of special interest to more applied research (i.e., Army needs) is the collection of microstructural data, which reveal features that directly influence a material's performance. One approach is the use of in-situ focused ion beam (FIB) pulsed-laser ablation for characterization of bulk 3D microstructures[9,10] In these systems, a femtosecond laser couples to a dual beam FIB, giving the advantage of removing larger volumes of material while maintaining the imaging resolution of an scanning electron microscope (SEM).

Microstructural features (e.g., grain and phase size and distributions) tend to strongly influence a material's performance. For example, the Hall–Petch effect is a well-known relationship between a material's strength and the average grain size. Additionally, the process-property-performance paradigm suggests that a microstructure is dependent on processing conditions,[11] which dictate how these features evolve. Characterizing these microstructural features is important as they are related to how a material will deform when subjected to mechanical work (i.e., for structural applications). Therefore, being able to quickly characterize these features is essential for accelerated materials discovery and processing optimization. Considering the importance of microstructural information, there has been significant development of frameworks to analyze highly indexed data (e.g., electron backscattered diffraction [EBSD] through DREAM.3D[12]). However, limited efforts have been devoted to developing tools that can reconstruct grayscale highly contrasted backscattered electron micrographs. While these data are not as information rich as EBSD data, they provide useful information that is faster to collect and more economic to store.

Grayscale micrographs are suitable for characterizing phase distributions of multiphase materials. Additionally, this type of mesoscale information is essential for computational models that aim to understand how a material responds to external stimuli (e.g., pressure). Hence, a systematic approach to characterizing grayscale-based microstructural information is presented. A Python script was developed to clean and analyze highly contrasted electron backscatter micrographs and build a Visualization ToolKit (VTK) readable file.[13] This file type can be further analyzed (e.g., phase clustering) in ParaView.[14] As a demonstration, the systematic analysis was used to analyze a silicon carbide (SiC) boron carbide (B_4C) ceramic composite. Understanding the distribution of the B_4C within the SiC matrix is important to understand its protective performance.

2. Image Collection

Coupons, $200\,\mu\mathrm{m}$ thick, of a commercially available SiC–B_4C composite were acquired following mechanical polishing to a final surface roughness of $20\,\mathrm{nm}$. A more detailed description of the sample alignment and sectioning procedure can be found in the report by Ligda et al.[15] In short, the sample mounts onto a piezo-based positioning stage and is then pre-tilted such that the desired sample face is parallel to the incoming laser beam. The laser is a Clark MXR-CPA with a wavelength of $775\,\mathrm{nm}$ and a pulse width of $150-200\,\mathrm{fs}$. For serial sectioning, a total of 120 slices were cut using a laser pulse energy of $13\,\mu\mathrm{J}$, scan speed of $33\,\mu\mathrm{m/s}$, and slice thickness of $1\,\mu\mathrm{m}$. Each slice takes on average approximately $3-5\,\mathrm{min}$ to laser cut and image, with the bulk of this time going to the former. Secondary electron images were taken of each slice at a magnification of $500\times$ (equivalent scan area of $256\times221\,\mu\mathrm{m}$) and electron beam settings of $20\,\mathrm{kV}$, $2.4\,\mathrm{nA}$. Due to the difference in atomic number between boron (B) and silicon (Si), the contrast and brightness of these images is adjusted so that the SiC phase is bright while the B_4C phase is dark. This binary type of image should be ideal for the later segmentation procedures.

3. Microstructural Analysis

One of the disadvantages of these grayscale images is that it is challenging to fully align layers based on intensity values. Moreover, this is complicated when fast scans and laser-induced periodic surface structures (LIPSS) form, which cause noisy micrographs.[16–18] Therefore, images must be *cleaned* in order to minimize any artifacts. The random walker segmentation algorithm,[19] as implemented in scikit-image,[20] was used to segment the micrographs into SiC and B_4C features. These segmented micrographs are then stacked to form a reconstructed microstructure. The reconstructed microstructures can be post analyzed to obtain information not attainable from 2D micrographs.

3.1 Image Segmentation

The random walker algorithm (RWA) relies on the labeling of "seed" pixels. Then, unlabeled pixels are imagined to have released "walkers", which have a given probability to reaching a labeled (seeded) pixel. Hence, the walker's probability of reaching a specific seed will determine the value that an unlabeled pixel will adopt. The RWA aims to minimize the "energy" (combinatorial formulation of the Dirichlet integral):

$$D[x] = \frac{1}{2}\int_{\Omega} |\nabla x|^2 d\Omega = \frac{1}{2}x^T L x = \frac{1}{2}\sum_{e_{ij}\in E} w_{ij}(x_i - x_j)^2, \tag{1}$$

where e_{ij} is the edge connecting two neighboring pixels, w_{ij} is the edge weighting function and x_i is a real-valued number for a given pixel. The edge weighting function encodes similarities between pixels, as is defined as,

$$w_{ij} = \exp\left(-\beta(g_i - g_j)^2\right), \tag{2}$$

where β is a free parameter and g_i is the pixel intensity. Grady[19] likens the objective of this algorithm to analyzing the steady-state (infinite time) diffusion equation.

Figure 1 shows the image analysis framework used in segmenting the micrographs into distinct phases. The *noisy* image shows the as-collected SEM where white and

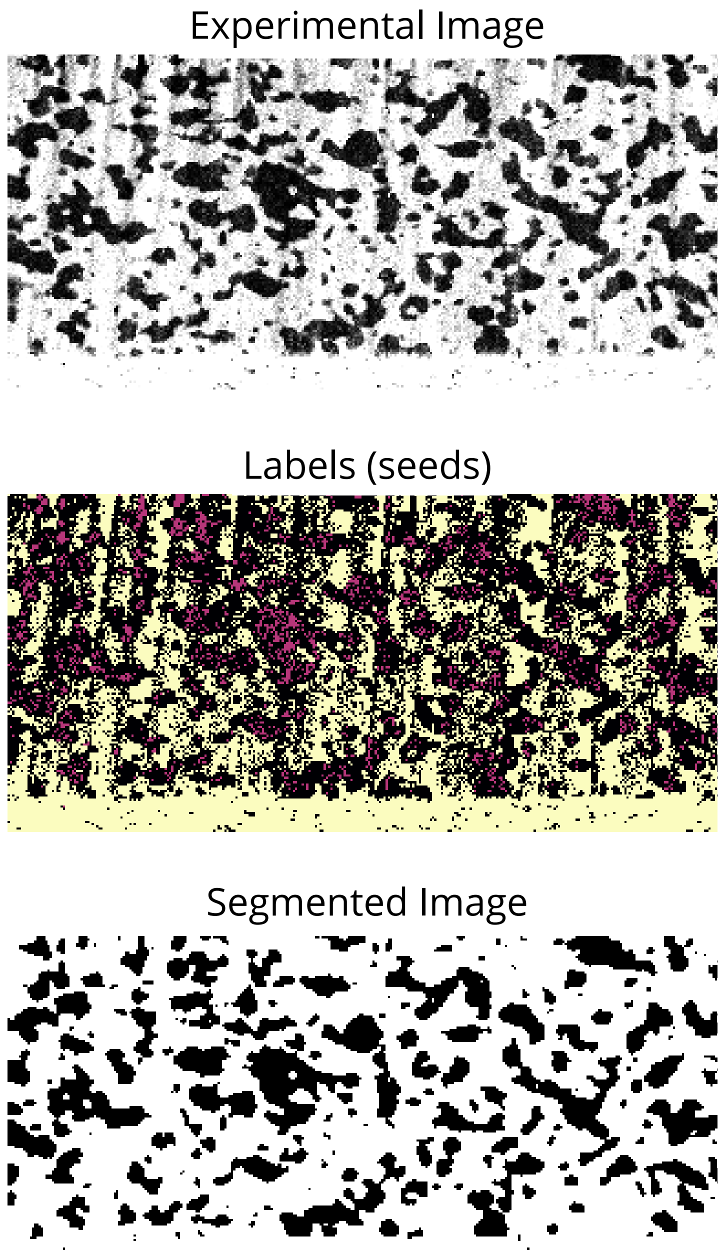

Fig. 1 Example of systematic approach for analyzing highly contrasted micrographs via segmentation

black regions correspond to SiC and B_4C, respectively. It also shows a significant number of gray regions, which arise intrinsically from the measurements. To seed the labels, the experimental images were first normalized as

$$\bar{g}_i = 2 \cdot \frac{g_i - \min(G)}{\max(G) - \min(G)} - 1, \tag{3}$$

where the G is the pixel intensity set and the projection results in the $\{g_i \in G : 0 \leq g_i \leq 1\} \rightarrow \{\bar{g}_i \in \bar{G} : -1 \leq \bar{g}_i \leq 1\}$ renormalization. To properly identify these as either SiC or B_4C, the noisy image is seeded with markers based on some criterion

$$s_i = \begin{cases} \text{dark/purple}, & \bar{g}_i \leq -g_c \\ \text{bright/yellow}, & \bar{g}_i \geq g_c \end{cases}, \tag{4}$$

where g_c is a cutoff pixel intensity. It should be noted that the black regions in the "labels" image in Fig. 1 are the unlabeled pixels from which walkers are "ejected" in search of a seed to adopt. This labeled image is then used by the RWA to segment the image into the distinct phases.

3.2 Stack Reconstruction and Analysis

The segmented images provide a planar 2D representation of the microstructure. To get a fully representative microstructure, these segmented micrographs were "stacked" onto each other. Due to the regular array nature of pixelated images, these were converted into a VTK image (VTI) file (i.e., a structured file). A representative stack of 20 micrographs is shown in Fig. 2 where the blue and red regions correspond to B_4C and SiC, respectively. It is shown that B_4C is fairly dispersed throughout the SiC matrix.

To better understand the microstructure, the stack was analyzed with ParaView's *Connectivity* filter. The B_4C's connectivity was analyzed on a 50-stack microstructure taken from a reduced region of the original data set. ParaView's Connectivity filter clusters voxels by assigning "connected components" (adjacent voxels) a given "region ID" (i.e., unique integer). The resulting connectivity is shown in Fig. 3, where a very large cluster (dark blue region) can be observed. The largest cluster can be filtered out by thresholding it's region ID, as shown in Fig. 3b. By comparing Fig. 3a and b, it is determined that the largest cluster is approximately 93% of the B_4C phase. Further thresholding isolates the smaller clusters (Fig. 3c).

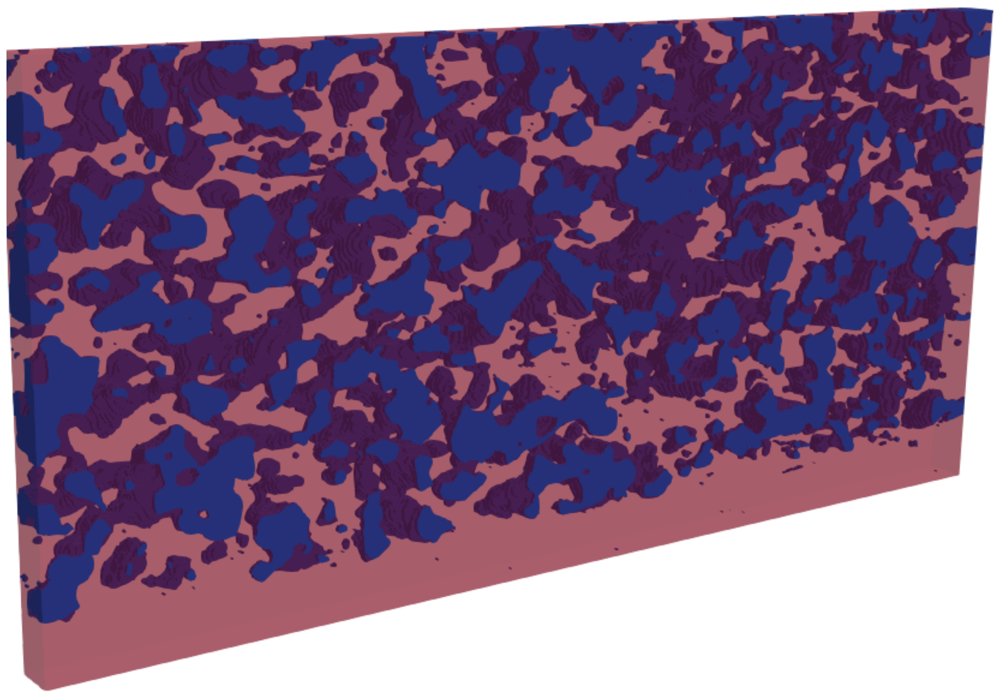

Fig. 2 Representative stack of 20 ablated layers of SiC (red) and B_4C (blue)

3.3 Comments on Post Processing

The analysis previously highlighted can be useful in determining important microstructural characteristics, but it is essential to properly treat these features. It should be noted that in order to obtain a large representative microstructure, large sectioning steps were used. While the X and Y resolution is fairly small ($\delta_{x,y}$ $\sim$0.125 µm), the sectioning steps were δ_z $\sim$1 µm. This can be observed in Fig. 4. This enables HiTpE data collection, but the large δ_z could result in artifacts. Avoiding these artifacts are of most importance when attempting to obtain representative feature topologies. For instance, smoothing the voxelized B_4C precipitate in Fig. 4 will result in very different-looking precipitates. This is shown for smoothing of the precipitates for different number of smoothening iterations. Clearly, the topology and overall precipitate size are influenced by the number of smoothening operations.

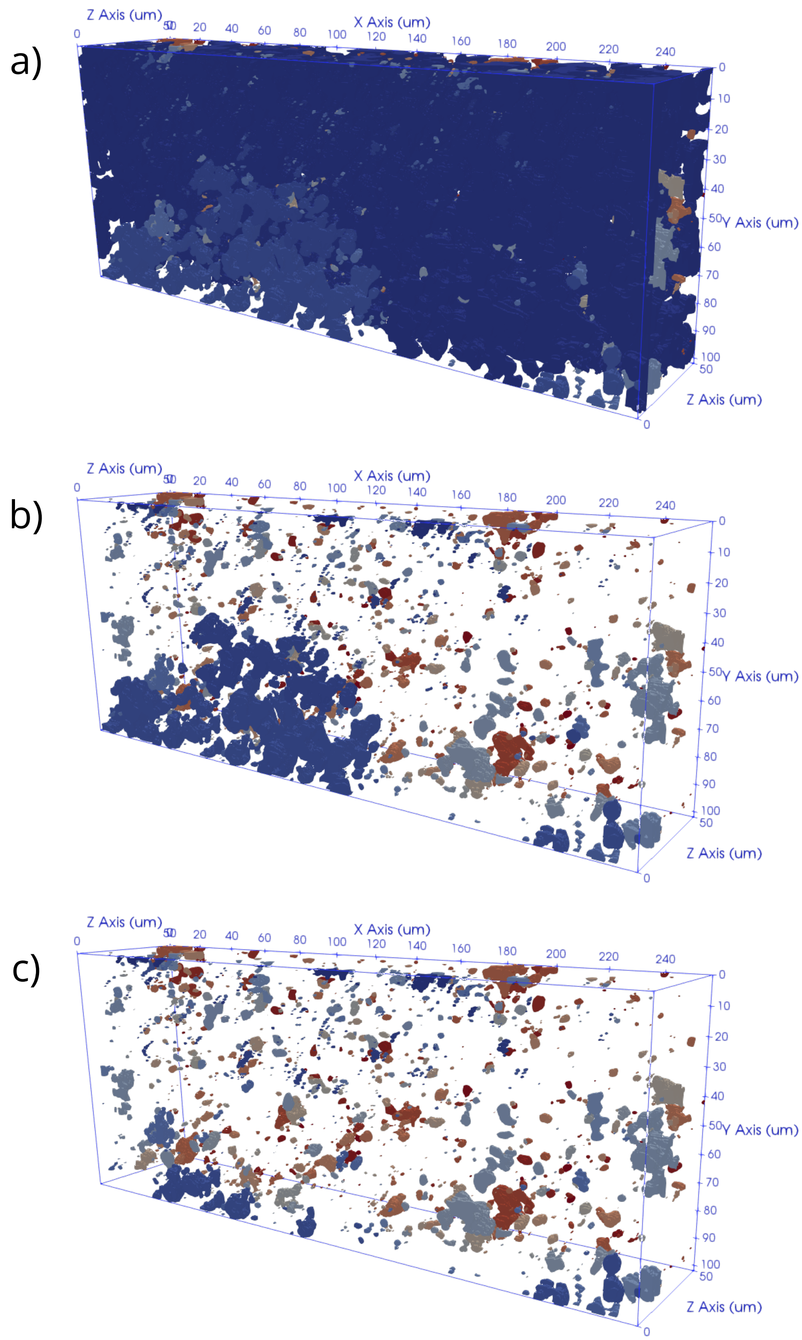

Fig. 3 Connectivity analysis showing the B_4C precipitate clusters. It is shown that a large fraction of the secondary phase is highly connected.

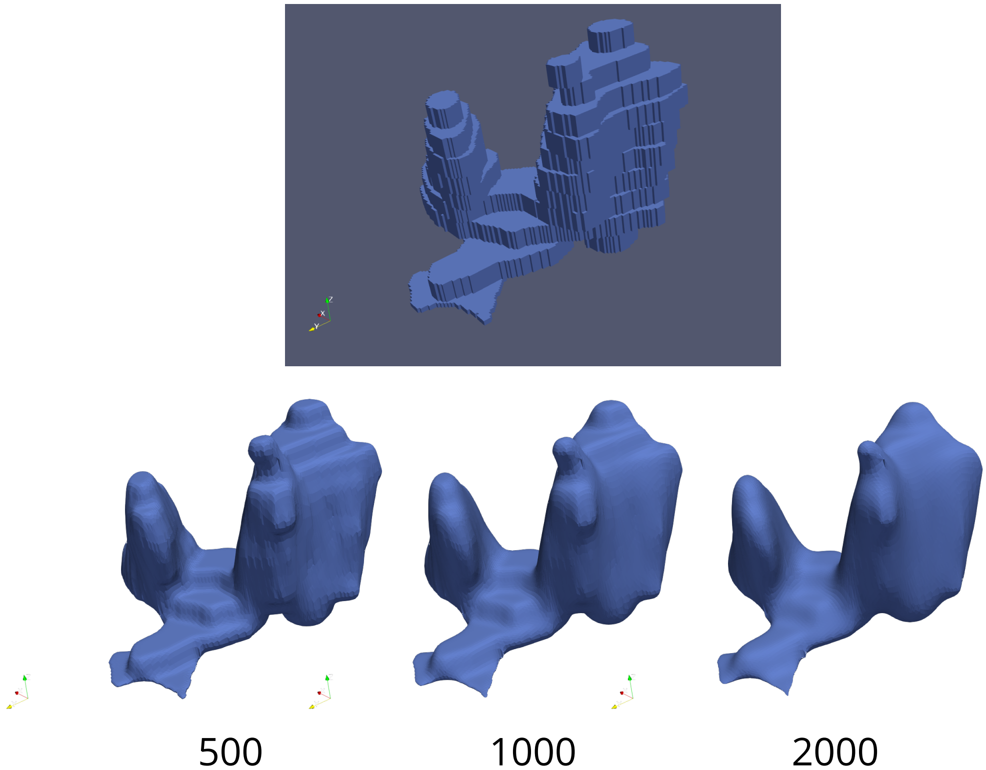

Fig. 4 Application of ParaView's smoothening filter. It is shown that the number of smoothening iterations can cause a feature's topology to change drastically

To showcase the importance of proper filtering, the B_4C precipitates resulting after 1000 and 2000 smoothening iterations are subjected to planar loads. The objective was to determine if the differences in post-processing would influence mechanical responses. These smoothed precipitates were imported as ParaView generated stereolithography (STL) files into the COMSOL finite-element analysis platform. Then, a SiC cuboid was overimposed, to enclose the precipitate with matrix material. Finally, planar loads ($\sigma_{\pm z} = 1\mathrm{N/m^2}$) were applied on the top and bottom surfaces of the SiC cuboid. The resulting strained microstructure are shown in Fig. 5. It is qualitatively shown that for fewer iterations, the SiC cuboid deforms more uniformly.

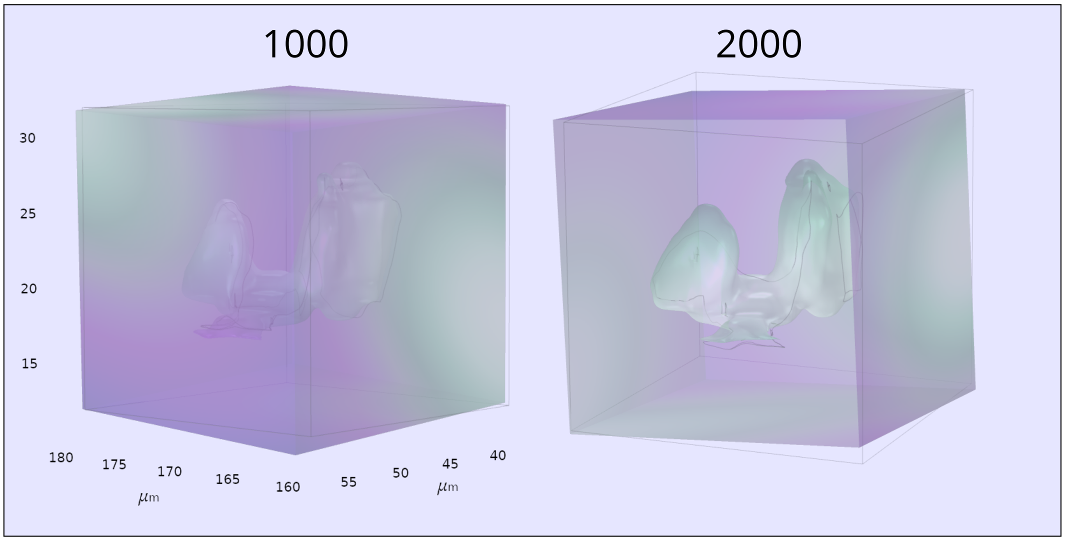

Fig. 5 SiC matrix deforms in drastically different forms depending on how the precipitate was smoothen

4. Conclusion

A systematic framework to analyzing grayscale reconstructed 3D microstructures is presented. It is demonstrated that the RWA is able to segmented highly contrasted micrographs, which then can be stacked into the reconstructed microstructure. These microstructures can then be post analyzed to characterize mesoscale features. For instance, it was shown that the vast majority of the secondary B_4C phase is connected into a large cluster. Furthermore, the importance of careful and consistent post-processing these microstructural features (e.g., smoothening of precipitate voxelated surfaces) is shown. Performing a simple micromechanical analysis on an isolated precipitate subjected to different smoothening iterations results in a different mechanical response.

5. References

1. Jain A et al. Commentary: The materials project: A materials genome approach to accelerating materials innovation. Apl Materials. 2013;1(1):011002.

2. Curtarolo S, Hart GL, Nardelli MB, Mingo N, Sanvito S, Levy O. The high-throughput highway to computational materials design. Nature Materials. 2013;12(3):191.

3. Executive Office of the President. Materials Genome Initiative for Global Competitiveness. Washington (DC): National Science and Technology Council; 2011 [accessed 2019]. https://www.mgi.gov/sites/default/files/documents/materials_genome_initiative-final.pdf

4. Green ML et al. Fulfilling the promise of the materials genome initiative with high-throughput experimental methodologies. Applied Physics Reviews. 2017;4(1):011105.

5. Sebba DS, Watson DA, Nolan JP. High throughput single nanoparticle spectroscopy. ACS Nano. 2009;3(6):1477–1484.

6. Ferrari AC et al. Raman spectrum of graphene and graphene layers. Physical Review Letters. 2006;97(18):187401.

7. Ohtani M et al. Concurrent x-ray diffractometer for high throughput structural diagnosis of epitaxial thin films. Applied Physics Letters. 2001;79(22):3594–3596.

8. Zarnetta R, Buenconsejo PJS, Savan A, Thienhaus S, Ludwig A. High-throughput study of martensitic transformations in the complete Ti–Ni–Cu system. Intermetallics. 2012;26:98–109.

9. Echlin MP, Mottura A, Torbet CJ, Pollock TM. A new TriBeam system for three-dimensional multimodal materials analysis. Review of Scientific Instruments. 2012;83(2):023701.

10. Echlin MP, Mottura A, Wang M, Mignone PJ, Riley DP, Franks GV, Pollock TM. Three-dimensional characterization of the permeability of W–Cu composites using a new "TriBeam" technique. Acta Materialia. 2014;64:307–315.

11. McDowell DL, Olson GB. Concurrent design of hierarchical materials and structures. In: Scientific Modeling and Simulations; Verlag Berlin Heidelberg (Germany): Springer; 2008; p. 207–240.

12. Groeber MA, Jackson MA. Dream. 3D: a digital representation environment for the analysis of microstructure in 3D. Integrating Materials and Manufacturing Innovation. 2014;3(1):5.

13. Schroeder WJ, Lorensen B, Martin K. The visualization toolkit: an object-oriented approach to 3D graphics. 4th ed. Clifton Park (NY): Kitware; 2006.

14. Ayachit U. The paraview guide: a parallel visualization application. Clifton Park (NY): Kitware, Inc.; 2015.

15. Ligda JP, Jordan W, Lorenzo N, Sano T, Schuster BE. Three-dimensional microstructural characterization using a femtosecond laser coupled focused ion beam microscope. Aberdeen Proving Ground (MD): Army Research Laboratory (US); 2018. Report No.: ARL-TR-8295.

16. Bonse J, Krüger J, Höhm S, Rosenfeld A. Femtosecond laser-induced periodic surface structures. J Laser Appl. 2012;24(4):042006.

17. Sedao X, Maurice C, Garrelie F, Colombier JP, Reynaud S, Quey R, Pigeon F. Influence of crystal orientation on the formation of femtosecond laser-induced periodic surface structures and lattice defects accumulation. Applied Physics Letters. 2014;104(17):171605.

18. Tan B, Venkatakrishnan K. A femtosecond laser-induced periodical surface structure on crystalline silicon. Journal of Micromechanics and Microengineering. 2006;16(5):1080.

19. Grady L. Random walks for image segmentation. IEEE Transactions on Pattern Analysis & Machine Intelligence. 2006;(11):1768–1783.

20. Van der Walt S, Schönberger JL, Nunez-Iglesias J, Boulogne F, Warner JD, Yager N, Gouillart E, Yu T. scikit-image: image processing in python. PeerJ. 2014;2:e453.

List of Symbols, Abbreviations, and Acronyms

1D	one-dimensional
2D	two-dimensional
3D	three-dimensional
B	boron
B_4C	boron carbide
EBSD	electron backscatter diffraction
FIB	focused ion beam
HiTp	high-throughput
HiTpE	high-throughput experimental
LIPSS	laser induced periodic surface structures
RWA	random walker algorithm
SEM	scanning electron microscope
Si	silicon
SiC	silicon carbide
VTI	Virtual ToolKit image
VTK	Virtual ToolKit

1 (PDF)	DEFENSE TECHNICAL INFORMATION CTR DTIC OCA	
1 (PDF)	FCDD RLD CL TECH LIB	
1 (PDF)	GOVT PRINTG OFC A MALHOTRA	
33 (PDF)	DIR CCDC ARL FCDD RLD H MAUPIN M TSCHOPP FCDD RLW A RAWLETT S SCHOENFELD FCDD RLW B R BECKER A TONGE FCDD RLW D B MCWILLIAMS J SOUTH L VARGAS-GONZALEZ FCDD RLW M J LASCALA B LOVE FCDD RLW MA D O'BRIEN FCDD RLW MB C FOUNTZOULAS A GAYNOR G GAZONAS E HERNANDEZ D HOPKINS J LIGDA B POWERS T SANO T WALTER FCDD RLW MC R JENSEN J SNYDER FCDD RLW MD K CHO FCDD RLW ME M GOLT A DIGIOVANNI J LASALVIA S SILTON FCDD RLW MF K DARLING R DOWDING A GIRI C HAINES	B HORNBUCKLE